Influence of the pore diameter in Cu/Co/Cu antidots: A XANES study

H. Garad, Suhail Usmani, D. Barral, P. David, L. Cagnon, D. Testemale, D. Mannix, F. Fettar, O. Proux, A. Rosa, et al.

Important Notice to Authors

No further publication processing will occur until we receive your response to this proof.

Attached is a PDF proof of your forthcoming article in Physical Review Materials. Your article has 15 pages and the Accession Code is **BP13310M**.

Please note that as part of the production process, APS converts all articles, regardless of their original source, into standardized XML that in turn is used to create the PDF and online versions of the article as well as to populate third-party systems such as Portico, Crossref, and Web of Science. We share our authors' high expectations for the fidelity of the conversion into XML and for the accuracy and appearance of the final, formatted PDF. This process works exceptionally well for the vast majority of articles; however, please check carefully all key elements of your PDF proof, particularly any equations or tables.

Figures submitted electronically as separate files containing color appear in color in the journal.

Specific Questions and Comments to Address for This Paper

1 Please provide zip code for 3rd affiliation.
2 In second affiliation, please check our expansion of Mto to Meteo.
3 Please define sublable(c) and (d) in Fig. 1.
4 Please check changed spelling in Fig. 2 to Anodization (2 times).
5 Please check changed to White in axis label.
6 Ref. [44]: Please update if paper has been accepted for publication. Please add preprint number if available.
7 Please check journal.
Q: This reference could not be uniquely identified due to incomplete information or improper format. Please check all information and amend if applicable.

Open Funder Registry: Information about an article's funding sources is now submitted to Crossref to help you comply with current or future funding agency mandates. Crossref's Open Funder Registry (https://www.crossref.org/services/funder-registry/) is the definitive registry of funding agencies. Please ensure that your acknowledgments include all sources of funding for your article following any requirements of your funding sources. Where possible, please include grant and award ids. Please carefully check the following funder information we have already extracted from your article and ensure its accuracy and completeness:
Ministry of Foreign Affairs (FR)

Other Items to Check

- Please note that the original manuscript has been converted to XML prior to the creation of the PDF proof, as described above. Please carefully check all key elements of the paper, particularly the equations and tabular data.
- Title: Please check; be mindful that the title may have been changed during the peer-review process.
- Author list: Please make sure all authors are presented, in the appropriate order, and that all names are spelled correctly.
- Please make sure you have inserted a byline footnote containing the email address for the corresponding author, if desired. Please note that this is not inserted automatically by this journal.
- Affiliations: Please check to be sure the institution names are spelled correctly and attributed to the appropriate author(s).
- Receipt date: Please confirm accuracy.
- Acknowledgments: Please be sure to appropriately acknowledge all funding sources.
- Hyphenation: Please note hyphens may have been inserted in word pairs that function as adjectives when they occur before a noun, as in "x-ray diffraction," "4-mm-long gas cell," and "*R*-matrix theory." However, hyphens are deleted from word pairs when they are not used as adjectives before nouns, as in "emission by x rays," "was 4 mm in length," and "the *R* matrix is tested."

  Note also that Physical Review follows U.S. English guidelines in that hyphens are not used after prefixes or before suffixes: superresolution, quasiequilibrium, nanoprecipitates, resonancelike, clockwise.
- Please check that your figures are accurate and sized properly. Make sure all labeling is sufficiently legible. Figure quality in this proof is representative of the quality to be used in the online journal. To achieve manageable file size for online delivery, some compression and downsampling of figures may have occurred. Fine details may have become somewhat fuzzy, especially in color figures. Figures to be published in color online will appear in color on these proofs if viewed on a color monitor or printed on a color printer.
- Please check to ensure that reference titles are given as appropriate.
- Overall, please proofread the entire *formatted* article very carefully. The redlined PDF should be used as a guide to see changes that were made during copyediting. However, note that some changes to math and/or layout may not be indicated.

Ways to Respond

- ***Web:*** If you accessed this proof online, follow the instructions on the web page to submit corrections.
- ***Email:*** Send corrections to prmproofs@aptaracorp.com
  Subject: **BP13310M** proof corrections
- ***Fax:*** Return this proof with corrections to +1.703.791.1217. Write **Attention:** PRM Project Manager and the Article ID, **BP13310M**, on the proof copy unless it is already printed on your proof printout.

PHYSICAL REVIEW MATERIALS **00**, 006000 (2018)

Influence of the pore diameter in Cu/Co/Cu antidots: A XANES study

H. Garad, S. Usmani, D. Barral, P. David, L. Cagnon, D. Testemale, D. Mannix, and F. Fettar
Université Grenoble Alpes, Institut Néel, F-38042 Grenoble, France

O. Proux
Université Grenoble Alpes, CNRS, IRD, Irstea, Météo France, OSUG, FAME, 38000 Grenoble, France

A. Rosa, O. Mathon, and S. Pascarelli
ESRF, Grenoble, France

(Received 23 February 2018; published xxxxxx)

Antidot materials, i.e., two-dimensional nanostructures with a periodic array of nanopores, are of great scientific interest due to their unique nanomagnetic properties and their potential application in storage devices. It is well known that physical properties of antidots are directly linked to the diameter of nanopores and their spacing, as well as to the morphology and the localizations of chemical species. However, due to their nanoscale size, their characterization remains challenging. Here, we present a detailed investigation of the morphology and presence of oxide species in antidots as a function of the pore diameter using polarized x-ray absorption spectroscopy. For this study we synthesized and characterized Cu(10 nm)/Co(12 nm)/Cu(10 nm) sputtered antidots, fabricated by the double-anodization technique assisted by atomic layer deposition. The pore size ranged from 20 to 80 nm, with a fixed interpore distance (105 nm). An unholed multilayer deposited on Si/SiO_2 was also investigated for comparison. We observed a clear correlation between the increase of pore diameter and the enhancement of oxide content from three different x-ray absorption near edge structure analysis methods. Polarized XAS allowed us to localize the CoO nanorings inside the pores. We propose that the CoO formation is directly related to the crescent shape of the multilayer deposit inside the pores. The coercivity of antidots is enhanced by increasing the magnetic atomic proportion in the periphery of nanopores. The structural observations were also used to develop a simple model in order to estimate the proportion of atoms inside the pores and on the top of the antidots as a function of the interpore distance, the hole diameter, and the penetration length of deposition inside the pores. This model can be easily used in the literature for estimating the atomic species deposited on antidots.

DOI: 10.1103/PhysRevMaterials.00.006000

I. INTRODUCTION

Nano-objects are of great industrial and scientific interest in many fields. Indeed, they present key elements employed in electronic devices using in particular magnetic elements. Nanocompounds studied over the last two decade are antidots or nanopores, which constitute two-dimensional nanostructures in geometrically ordered arrays presenting the counterparts to dot nanostructures [1–4]. The physical properties of antidots are known to be directly linked to both the diameter of nanopores and to their spacing, which represent the key parameters in the design of antidots for industrial applications (see [5] for review).

Magnetic properties of antidots have received widespread attention due to their applications in magnetoresistance [6] and magnetic hardening [7–10] effects, high density data storage [11,12], and magnetic devices [13–15]. They bear several advantages over the conventional dots system, including the absences of a super-paramagnetic lower limit of the bit size, the preservation of magnetic properties, large-area fabrication at low cost, and the absence of damage caused by nanofabrication processes. Several previous studies aimed at establishing the relation between the antidot size and distribution to the nanomagnetic properties; see for example [7–10] and references therein. This foregoing research has been limited to antidots with relatively large pore size (d) of around 0.1–20 μm and with interpore distances (p, periodic array) of 0.2–50 μm, by implementing physical synthesis methods [7–11,16,17]. However, in order to reach magnetic recording properties that are suitable for industrial applications, small pore sizes below $<$100 nm together with a sufficiently large p value of $\approx$100 nm are required [12], leading to a p/d ratio higher than 1.

The pioneer work of Masuda *et al.* [18] has enabled the fabrication of ordered pore sizes below 100 nm using a two-step-anodization method. The choice of acid solution presents a key factor in this process as it determines the resulting d and p of the antidot array. The use of sulfuric acid in the anodizing process induces low d and moderate p values of typically 7–46 nm and 60 nm, respectively [19]. Oxalic acid in turn leads to both higher d and p values of 35–66 nm and 105 nm, respectively [20]. Although this method clearly achieves d values below 100 nm, its major limitation is the strong coupling between d and p values, which both increase linearly with the anodizing potential. It is therefore impossible to constantly reduce the pore diameter by keeping the interpore distance constant using this chemical method.

For real industrial applications, such as data storage, the pore dimensions have to be reduced to a few nanometers while maintaining a weak coupling between pores. The ratio p/d

should be far ideally greater than one [21] for this situation to occur. However, the practical realization of such antidot structures, with a highly ordered arrangement of pores, remains extremely challenging and only a few studies have realized such antidots to date. For example, Chuang *et al.* [22] reported on multilayered Co/Cu/NiFe porous films with $d = 12$–17 nm and $p = 26$–40 nm by using a block copolymer template. Unfortunately, this technique requires multiple steps, including heat treatment and reactive ion etching that result in a weak p/d ratio close to 2. In comparison, elevated p/d ratios of up to 9 have been recently realized by Rahman *et al.* [19] on antidots with very small hole diameters of $d \approx 7$ nm and with p close to 60 nm. However, these antidots remain structurally problematic as their pore distribution is not perfectly hexagonal, the pore opening shapes are not circular, and the thickness of the alumina membrane is very thin (0.5 μm). Present synthesis methods need to be refined in order to achieve highly ordered and round-shaped antidots with low d values (several nm) and simultaneously high p values (at least 100 nm).

In this paper, we have implemented a method to fabricate pores size in the thick alumina substrate (60 μm) of Cu/Co/Cu antidots ranging between 17 and 78 nm at a constant p value of 105 nm (p/d ratio ranging from 1.4–6.2). This synthesis procedure is based on the two-step-anodization method combined with an additional atomic layer deposition step [21]. The high p/d ratios of antidots achieved with the present approach meet the demands of nanodevice applications. Local structural and chemical information has been obtained from quantitative x-ray absorption spectroscopy in the XANES (x-ray absorption near edge spectroscopy) range. Indeed, among the common structural characterization methods, such as scanning electron microscopy [12,19,20,23–37], atomic force microscopy [20,32,38–40], x-ray diffraction [29,30], and Rutherford backscattering spectroscopy [34,36], only a few investigation tools such as XANES, as well as transmission electron microscopy [12,19,31,33,35,38], allow us to distinguish the chemical nature of materials on the surface of antidots from those around the periphery of the nanopores.

In our work, we found that Co atoms are oxidized mainly around the inner pore rims forming therefore CoO nanorings. This result is is in agreement with findings of previous studies on the oxidation of Co and Fe in ultrathin metallic layers [41–43]. We also found a linear relationship between the pore diameter and the atomic fraction of oxide rings, allowing us therefore to tune the oxide part during the synthesis. Moreover, we have developed a simple model to spatially localize the Co and CoO components in our antidots using the observations made from our XANES data as well as atomic force microscopy (AFM) observations. Furthermore, our model allows a quantitative determination of atoms around the pores as well as on the antidot surface, which is of great potential interest to the community employing antidots. This morphological and structural information is crucial for the understanding of magnetic properties of antidots [44], as well as other physical properties reported in the literature on these materials, and is therefore of great interest for antidot applications in general.

The present paper is organized as follows: Section II employs experimental synthesis methods, and structural characterization techniques of antidots are described. Section III describes results on the quantitative analysis of the CoO content from x-ray absorption spectroscopy. Section IV is dedicated to the local structure and morphology of antidots from AFM and polarized XAS observations. Finally, in Sec. V, a model is presented to describe the structural and morphological properties of antidots which are directly related to their magnetic properties such as the coercivity. A very simple model is developed to calculate the proportions of atoms deposited on both the top and the periphery of pores.

II. EXPERIMENTS

A. Antidot preparation

In order to prepare antidot arrays, an anodic alumina membrane (AAM) was prepared by the two-step anodization process [18]. After mechanically polishing to a mirror-like aspect and electropolishing at 30 V for 2 minutes in a perchloric acid/methanol mixture (1/4 in volume) at 0 °C, high-purity (99.999%) aluminum foils were anodized in a 0.5 M oxalic acid with a constant potential of 40 V and temperature around 16 °C. The first and second anodizations were performed during 17 h and 7 h, respectively, which led to templates with a thickness of 60 μm, and hole diameter and interpore distance of 40 and 105 nm, respectively. Then a pore opening/widening treatment in a phosphoric acid solution at 35 °C was applied during an etching time (t_{etching}) that was varied between 30 and 90 minutes. This procedure permitted us to obtain a pore diameter larger than the native diameter which is close to 40 nm for 30 minutes etching time. In order to obtain pores with a diameter smaller than the native one, an alumina deposit was performed using atomic layer deposition (ALD) in exposure mode, with trimethylaluminum and water as precursors [21]. Two native samples were selected where the hole diameter was further reduced by applying two ALD cycles numbers ($\text{Nb}_{\text{cycles}}$) of 75 and 100. Finally, Cu(10 nm)/Co(12 nm)/Cu(10 nm) trilayers were sputtered on all templates to obtain the antidot arrays. Such multilayer compositions exhibit exchange bias effects at low temperature and double magnetic loops, as identified for example in [Cu(10 nm)/Co(8 nm)/Cu(10 nm)] [41]. Additionally, during the deposition of the antidot arrays, a substrate of Si/SiO_2 was used to produce continuous trilayers for comparison. In order to provide one unique batch of samples with similar substrate properties the sputtering process was performed on all 7 substrates at the same time, with a base pressure of approximately 6.0×10^{-8} mbar, an argon pressure of 3.0×10^{-3} mbar, a deposition temperature of around 20 °C, and deposition rates of 0.05 and 0.10 nm/s for Co and Cu, respectively.

B. Electron microscopy

After the multilayer sputtering process, all samples were analyzed using scanning electron microscopy (SEM) to measure the pore diameter and the interpore distance. Figure 1 shows top view images of four selected Cu/Co/Cu samples having different d values. We observed for all samples a hexagonal arrangement of holes with a constant periodicity of ≈105 nm in good agreement with what is commonly obtained with the two-step anodizing procedure in oxalic acid at 40 V. The ALD-treated template ($\text{Nb}_{\text{cycles}} = 100$) [Fig. 1(a)] clearly

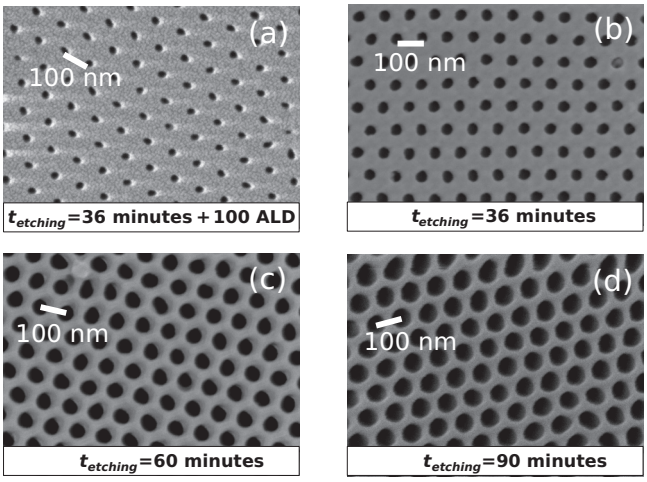

FIG. 1. SEM images of Cu(10 nm)/Co(12 nm)/Cu(10 nm) sputtered on alumina membranes with different pore diameters, where the etching time $t_{etching}$ is indicated. For the lowest $t_{etching}$ [36 minutes, panel (b)], an atomic layer deposition process was added to the double-anodization process, with 100 as the number of ALD cycles, leading to a reduction of the pore diameter (a).

displays a strong reduction of pore diameter from 42.6 nm [Fig. 1(b)] down to 17.0 nm [Fig. 1(a)].

Figure 2 summarizes the evolution of the hole diameter d as a function of deposition parameters. Here, d values in the range from 42.6–78.2 nm are plotted as a function of $t_{etching}$ in the bottom right part, while the top left part of Fig. 2 shows the relation of low d values (17–42.6 nm) as a function of Nb_{cycles}. A linear relationship is found between d and Nb_{cycles}, as well as between d and $t_{etching}$ at least up to $t_{etching} = 70$ minutes. We found $d \approx 1.08(\pm 0.01) + 0.09(\pm 0.01) \times t_{etching}$ for $t_{etching}$ in the 36–70 min range and $d \approx 42.3(0.7) - 0.24(0.01) \times Nb_{cycles}$ for $t_{etching} < 36$ min. The linearity of pore diameter with pore widening time has been already described for (Co/Pt)

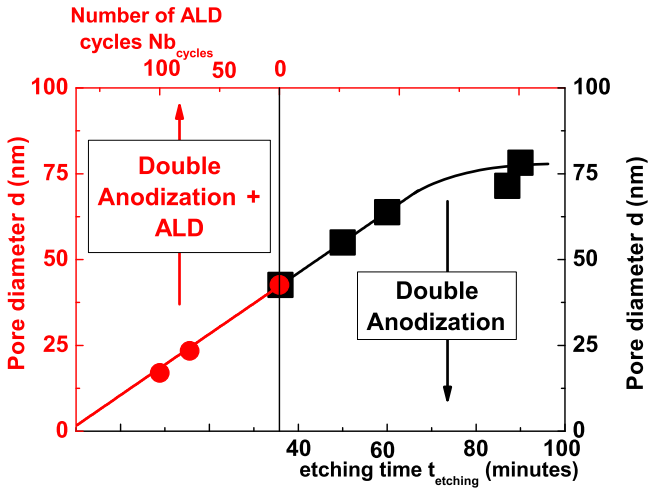

FIG. 2. Pore size d versus etching time $t_{etching}$ (bottom right) and versus Nb_{cycles} (top left) for Cu(10 nm)/Co(12 nm)/Cu(10 nm) sputtered on alumina membranes. The low d values (<40 nm) are obtained by combining double-anodization and atomic layer deposition techniques.

perpendicular antidot arrays [19]. In our study, a saturation of hole diameter seems to occur for the high $t_{etching}$ regime above 70 minutes evidenced by the deviation from the linearity between d and $t_{etching}$. We therefore conclude that the double-anodization technique using such fabrication of membranes does not allow obtaining d values greater than ≈80 nm as observed in Refs. [25,26]. Indeed, the reason that may lead to a saturation of d is the space available between two consecutive holes, which is $p - d$ where p is close to 100 nm. By increasing d and keeping constant p, this distance is reduced up to 0. Consequently, d reaches a maximum value for a network with a fixed p parameter, around $d = p \approx 100$ nm. Here, the maximum d value reaches ≈80 nm lower than the previewed one, indicating that the stabilization of the hexagonal network is stabilized up to 80% of the maximum value.

C. XAS

We employed polarized x-ray absorption spectroscopy in order to study in detail the Co-oxide layer forming inside the pores on the ultrathin deposition layers, as developed in Refs. [42,43]. X-ray absorption spectroscopy (XAS) is a powerful technique to provide information on the local chemical and structural environment of selected chemical species. In particular, the x-ray absorption near edge structure (XANES) is sensitive to the symmetry and the three-dimensional arrangement of neighboring atoms surrounding the absorbing atom. Polarization-dependent XANES measurements additionally allow the possibility of distinguishing between bonding characteristics in the plane of the surface and those perpendicular to it (linear dichroism).

XAS measurements at the Co K edge (7.71 keV) were conducted at the French CRG beamline BM30B and the beamline BM23 at the ESRF (Grenoble, France) using a double-crystal monochromator equipped with two Si(220) and two Si(111) crystals, having an energy resolution of approximately 0.4 eV and 1 eV, for BM30B and BM23, respectively. The energy was scanned between 7650 eV and 8550 eV. On BM23, ionization chambers filled with appropriate gas mixtures were used to measure the incoming beam intensity. On BM30B this measurement was ensured using Si photodiodes collecting photons scattered by a Kapton foil. Emitted fluorescence signals were detected using a 30 and a 13 element germanium solid state detector at BM30B and BM23, respectively, placed at 90° from the incoming beam. Bulk Co, CoO, and Co_3O_4 references were also used for comparison. For all measurements, the energy calibration of the two beamlines was done with the same method by measuring the XAS spectrum of a Co metallic foil. For the angular measurements, the sample was mounted on a precision goniometer and rotated from normal incidence by 45° and 80° (see Fig. 3). These measurement geometries allowed sampling an average of chemical bonds oriented parallel and perpendicular to the surface ($\alpha = 45°$ rotation) as well as bonds oriented mainly perpendicular to the antidot surface [$\alpha = 80°$ rotation, Fig. 3(c)] (see red arrows indicating probed bonding direction in Fig. 3). Here, the angle is defined between the electric field vector ($\vec{\epsilon}$ in green in Fig. 3) of the linear polarized incoming x-ray beam and the surface of the aluminum template. After background subtraction of the absorption spectra by linear extrapolation of the pre-edge

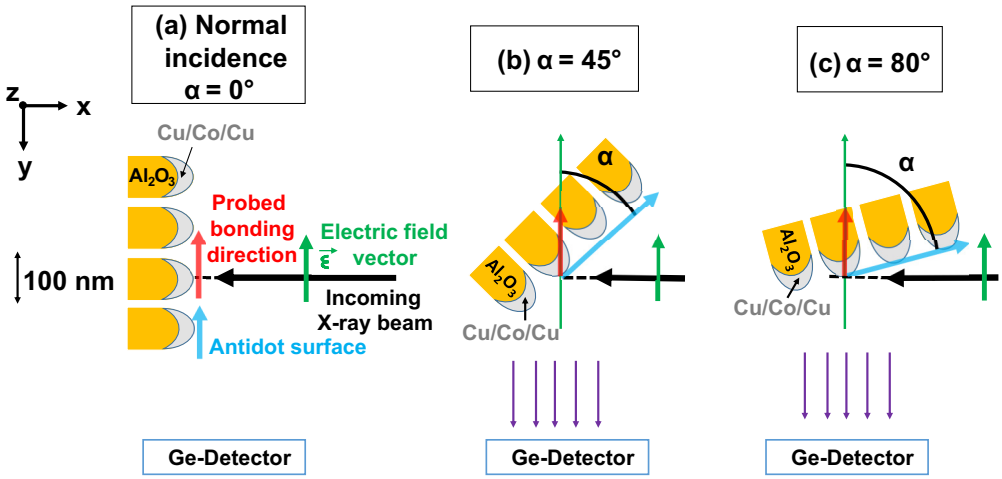

FIG. 3. Schematic view of the measurement geometries employed for polarized XAS. The alumina template is represented in yellow with a pore diameter of 50 nm and interpore distance of 105 nm (scale is shown on the lower left). The Cu/Co/Cu deposition appears in gray (thickness not at the scale). The angle α is defined between the electric field vector ($\vec{\epsilon}$ in green) of the linear polarized incoming x-ray beam and the surface of the aluminum template (blue arrow). In normal incidence geometry α equals 0° and the bond directions (red arrows) probed are parallel to the surface (a). For the present experiments, α was set to 45° and 80° to probe an average of bond directions perpendicular and parallel to the surface [panel (b), $\alpha = 45°$] and only those bonds oriented almost perpendicular to the template surface [panel (c), $\alpha = 80°$].

region, the spectra were normalized in the high energy range [extended x-ray absorption fine structure (EXAFS), not shown here] using the program Athena [45]. In the following, first measurements conducted at 45° are discussed and in the second part compared with those obtained at 80°.

III. QUANTIFICATION OF OXIDE CONTENT

Figure 4 shows the normalized Co K-edge XANES spectra obtained at $\alpha = 45°$ for the six nanosubstrates with different antidot pore diameters d together with the bulk reference spectra including Co, CoO, and Co_3O_4. The three insets in Fig. 4 highlight specific XANES regions in which spectral features change significantly with increasing pore diameter.

A first observation is the good agreement between the absorption signals of the unholed sample (pink spectra Fig. 4, continuous multilayer) with the one of pure bulk Co (red spectra Fig. 4). This agreement suggests a majority of Co-Co bonds in the Co layer most likely due to the enhanced thickness (12 nm). We note, however, that Co-Cu bonds cannot be distinguished as those elements have very similar scattering amplitudes. Another important observation is the continuous change of distinct XANES features with increasing pore diameter highlighted in Fig. 4 with letters A (pre-edge), B (white line), and D (first EXAFS oscillations). Starting from these features, the sample spectra evolve progressively from the Co metal spectrum (red) towards the CoO bulk spectrum (black). Interestingly, the normalized absorption signal of all spectra coincide at certain energies (i.e., point C and other points). This indicates that these are isosbestic points and that all sample spectra are related linearly to the two reference spectra via differences in concentration and therefore contribution to the total absorption signal, within the uncertainty of the possible Co-Cu bond. The observation on the XANES features suggests that Co metal dominates in the substrate layers, and that the increase of d progressively leads to the oxidation of the Co layer and formation of CoO. As proposed in [41], the oxidation process could be preferentially favored in the vicinity of the antidot, where the overall thickness of the trilayer is reduced due to the crescent shape gradient in thickness of the deposit. This particular crescent shape of the membrane around pores is also reported in Refs. [46,47]. It is therefor likely that the oxidation is preferentially located in the vicinity of the opening of the nanopores, where the covering of the protective Cu layer is reduced.

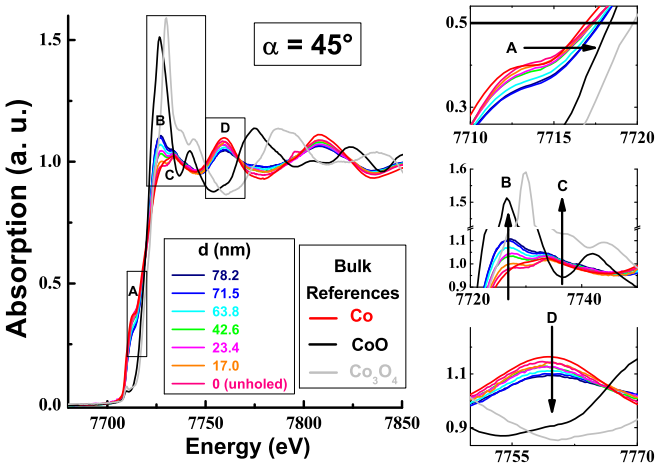

FIG. 4. Normalized Co K-edge XANES spectra of antidots with different pore size d, as well as the bulk CoO and Co metal reference spectra collected at $\alpha = 45°$. Letters from A to D delineate spectral regions of interest that are zoomed in the inlets on the right side. Black arrows in the inlets delineate the evolution of XANES spectra with increasing pore diameter d (from orange to blue). Note the similarities between the unholed sample (pink) and the Co metal reference (red) as well as the divergence of sample spectra towards the CoO reference spectra (gray) with increasing pore size.

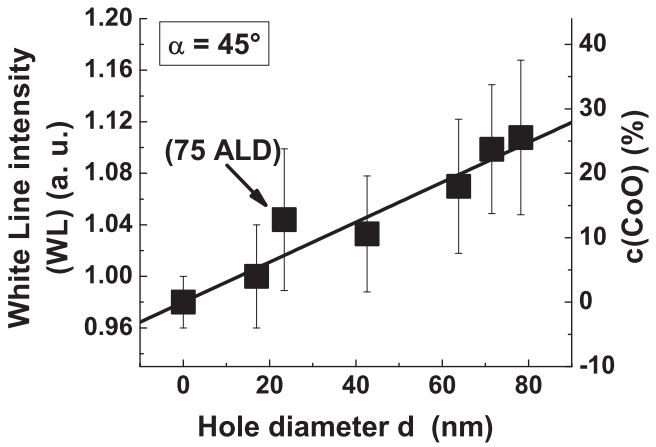

FIG. 5. White line (WL) intensity of the normalized Co K-edge sample spectra as a function of pore diameter d (left y axis) deduced from Fig. 4. The right y axis presents the extracted concentration of oxide content c(CoO) versus pore diameter d assuming a progressive oxidation of metallic Co in the nanopores. $d = 0$ corresponds to the unholed multilayer, the angle α (between $\vec{\epsilon}$ and layer plane) being equal to 45°.

These progressive changes in the XANES characteristics can be used to extract the volumetric proportions between Co and CoO in the antidots. Presently, only a few studies report on such qualitative and quantitative XANES investigations of thin layers composed of metallic and oxidized Co [42,44], while far more studies exist on Fe and FeO bearing thin layers (see for review [43]). Common methods to determine the degree of oxidation in nanometric multilayers are the compassion of sample spectral shifts in white line intensity and edge energy position compared to standard spectra. These methods have been for example used in Refs. [43,48] to quantify the oxide fraction of ultrathin iron and cobalt layers (8 Å and 6 Å), respectively. Another method is the linear combination fitting of the entire XANES region, which has been recently applied for Co thin films (4–20 Å) grown on $\alpha - Fe_2O_3(0001)$ single crystals [42]. We have employed all three methods to extract the oxide content from experimental spectra (first 45° and then 80° geometry) which also allowed evaluating their reliability.

A. White line analysis

The progressive increase of the white line intensity (WL) of sample spectra (see B in Fig. 4) was used to determine the fraction of CoO [c(CoO)] as a function of the pore diameter d (Fig. 5) following the procedure of Ref. [42]. The left side of Fig. 5 plots the extracted absolute WL intensities of normalized sample spectra versus the pore diameter, revealing a linear relationship. In order to estimate the oxide content, we used the maximal WL intensities of the pure Co metal spectra (normalized $\mu = 0.98$ at 7727.6 eV) and the CoO bulk spectra (normalized $\mu = 1.5$ at 7727.0 eV) as references for oxide contents of 0 and 100%, respectively (see second inset in Fig. 4). Next, a linear variation between WL and c(CoO) was assumed with $\mathrm{WL} = 0.53 \times 10^{-2} \times c(\mathrm{CoO}) + 0.98$. Resulting c(CoO) for the different substrates are plotted on the right vertical axis in Fig. 5, which can therefore be directly related to the pore diameter d.

The oxide fraction c(CoO) deduced from WL intensity analysis decreases linearly from 24.2(±1)% to 5.3(±1)% for the substrates with the largest and smallest pore diameters ($d = 78.2$ nm and 17.0 nm), respectively. A particular point in Fig. 5 is the sample with $d = 23.6$ nm (corresponding to $\mathrm{Nb_{cycles}} = 75$), which deviates from the linearity. For this antidot Co is slightly more oxidized than the substrate with larger pore diameter $d = 42.6$ nm. Indeed, the sample $d = 42.6$ nm has been employed as template for the atomic layer deposition (ALD) of the sample $d = 23.6$ nm. The deviation from linearity may suggest that oxidation of Co around pores is favored for samples treated additionally with ALD after the double-anodization process. A simple linear relation between c(CoO) and d [Eq. (1)] can be deduced (see the straight line in Fig. 5):

$$c(\mathrm{CoO})(\%, \pm 1) = 0.31d, \qquad (1)$$

which highlights the direct relationship between the antidot pore diameter and the degree of Co oxidation. This result is not obvious at first sight. As an explanation, we propose the fact that CoO atoms are preferentially localized around the valley of nanoholes. As a consequence, more the larger the diameter is, the more the CoO content is enhanced. A quantitative model justifying this hypothesis will be introduced in the next part of this study (see Sec. V).

B. Edge energy analysis

In a second step the variation of the edge energy (here referred to as E_{edge}, defined as normalized $\mu = 0.5$) was used as to derive the degree of oxidation in the samples. In general, a shift of the absorption edge to higher energies is either an indicator for an increase of the overall oxidation state of the element [43] or a modification of the interatomic bonding environment. In our samples we observed a continuous shift of the edge energy to higher energies with increasing d (see A in Fig. 4). This progressive shift can be interpreted qualitatively with the increasing degree of Co oxidation, in agreement with observed changes in the WL intensities (B in Fig. 4). In Fig. 6 the position of the edge energy as a function of the pore diameter d is shown, revealing again a simple linear relation. Similarly to the method developed above for the white line, we consider a simple linear variation between E_{edge} and c(CoO), where pure Co [c(CoO) = 0%] corresponds to E_{edge} for the Co bulk structure (7716.91 eV), since no CoO is detected. The extreme case where Co is fully oxidized [c(CoO) = 100%] is represented by E_{edge} of the bulk CoO (here 7718.37 eV). Using the assumption that the oxidation of Co is of the form of bulk CoO, c(CoO) is expressed as $c(\mathrm{CoO}) = 68.49 \times (E_{\mathrm{edge}} - 7716.91)$ [here 68.49 is coming from $(100 - 0)/(7718.37 - 7716.91)$]. Using this assumption, the content of CoO is found to be 37.7%, for the $d = 71.5$ nm membrane, which is 50% higher than the value obtained from the analysis of the white line (≈25%;). The replacement of the pure metallic Co standard with the unholed sample spectrum ($E_{\mathrm{edge}} = 7717.25$ eV) resulted in even higher c(CoO) values (≈49% for $d = 78.2$ nm). Such high degrees of oxidation in the samples seem however unrealistic considering that XANES

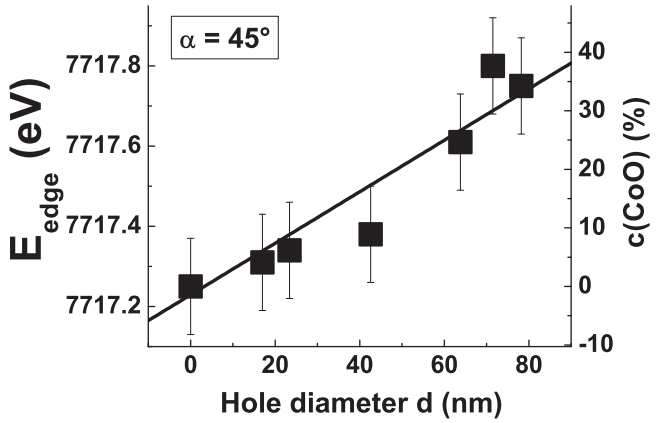

FIG. 6. Position of the Co K-edge energy E_{edge} as a function of pore diameter d (left y axis) deduced from Fig. 4 for normalized sample spectra of Cu/Co/Cu antidots. The right y axis presents the extracted concentration of oxide content c(CoO) versus pore diameter d assuming a progressive oxidation of metallic Co in the nanopores. $d = 0$ corresponds to the unholed multilayer, the angle α (between $\vec{\epsilon}$ and layer plane) being equal to 45°.

spectra from all samples are closer to the one of metallic Co. The latter suggests that Co metal dominates by far in the substrate layers. Therefore only the bulk metallic Co spectrum was used to deduce a linear variation between c(CoO) and d, which is shown in Fig. 6 on the right and which can be expresses as [Eq. (2)]

$$c(\text{CoO})(\%,\pm 2) = 0.44d - 1.44. \quad (2)$$

The comparison of results obtained from variations in WL intensity and edge energy position reveals that the E_{edge} analysis most likely overestimates values of c(CoO). This observation likely stresses the fact that the energy position variation of the XAS peaks does not depend linearly on the oxidation state. The second point is the improved linearity between c(CoO) and d by using the WL method. However, in contrast to results obtained from WL intensity fitting (Fig. 4), samples fabricated by ALD show no clear deviation from linearity between c(CoO) and d for the E_{edge} analysis (Fig. 5). We conclude that the discrepancies between these two methods may reflect the differing sensitivities of the two XANES features to modification of the interatomic bonding environment of the Co substrate inside the pores. Our results suggest that the edge energy may be affected to a greater degree than the WL intensities. A detailed understanding of how changes in the bonding environment and oxidation state affect distinct XANES features can be obtained from full multiple scattering calculations (FDMNES [49] or FEFF9 [50]) which are however out of scope of the present study and will be presented elsewhere.

C. Linear combination fitting

In contrast to the previous two methods (WL and edge energy), linear combination fitting (LCF) takes into account the total absorption signal over a distinct energy range and not only a certain energy or intensity position. In LCF the total absorption of the experimental sample spectrum is remodeled using the linear combination of reference spectra. For the LC fitting of sample spectra we followed established procedures [42,43] to extract the oxide content in the Co thin layer as a function of pore size. The normalized XANES sample spectra were fitted in the energy range between 7700 and 7830 eV using one Co metal and one Co-oxide reference spectrum each. The LCF was performed using the program Athena [45], which calculates the relative proportions of end-member spectra in the sample spectra using the following relation [Eq. (3)]:

$$\chi(E) = c(\text{Co})\chi_{\text{Co}}(E) + c(\text{Co oxide})\chi_{\text{Co oxide}}(E), \quad (3)$$

where c(Co) and c(CoO) are the Co and CoO contents expressed in percent. Since Co is either metallic or oxidized, the relation $c(\text{Co}) + c(\text{Co oxide}) = 1$ is satisfied. We tested different reference spectra, including bulk Co metal, the unholed Co substrate, CoO bulk, CoO thin film (1.5 nm thickness from Ref. [48]), as well as Co_3O_4 bulk. The two standard compounds that fit best the sample spectrum were evaluated from the χ^2 parameter, which is an indicator for the quality of the fit. Because the measurement uncertainty is difficult to assess for XANES data and the quantification of the independent number of points is not feasible in XANES the absolute value of χ^2 cannot be used to evaluate the quality of the fit. Relative changes in χ^2 can however be used to determine the best fit from a set of fits. Therefore, a relative reduction of χ^2 will indicate whether employed reference compounds are representative for the sample. For the evaluation of the best reference compounds we used the sample spectrum with the highest expected degree of oxidation, i.e., the sample with the greatest pore diameter (78.2 nm). The fitting results of different combinations of reference spectra are presented in Fig. 7, the nature of references being indicated in each graph. χ^2 values and fractions of reference compounds are summarized in Table I.

For the oxide component we found that fits with the Co_3O_4 standard are generally of poor quality compared to the measured data [Fig. 7(a) and Fig. 7(b)] and exhibit χ^2 values (>0.3) much higher than ones obtained by using CoO, suggesting that this is not a component present in the sample. This finding is consistent with our previous analysis from Fig. 4. The replacement of Co_3O_4 with CoO bulk improves significantly the fit quality and reduces the χ^2 value in the (0.03–0.05) range [Fig. 7(c) and Fig. 7(d)]. The CoO thin layer reference (1.5 nm) spectrum [Fig. 7(e) and Fig. 7(f)] in turn gives very close fitting results compared to the CoO bulk reference, giving only a slightly higher χ^2 value in the (0.05–0.08) range. However, a small deviation of the fit compared to the measured spectrum in the white line region is apparent when the CoO thin layer spectrum is employed, as revealed by arrows in Fig. 7(e) and Fig. 7(f). The CoO thin layer spectrum was obtained from a Pt-Co and CoO-AlO_x multilayer substrate reported in Ref. [48]. Additional Co bonding environments such as Pt-Co and Co-Al in the absorption signal of the CoO thin layer spectrum, which are not present in our samples, may explain the lower quality of fits compared to the CoO bulk spectrum. This is the reason why a CoO bulk is favored for the adjustment of XANES data.

For the metallic component, we obtained best fitting results by employing the unholed spectrum as the end member [see Fig. 7(d)] compared to ones with the Co bulk spectrum [see

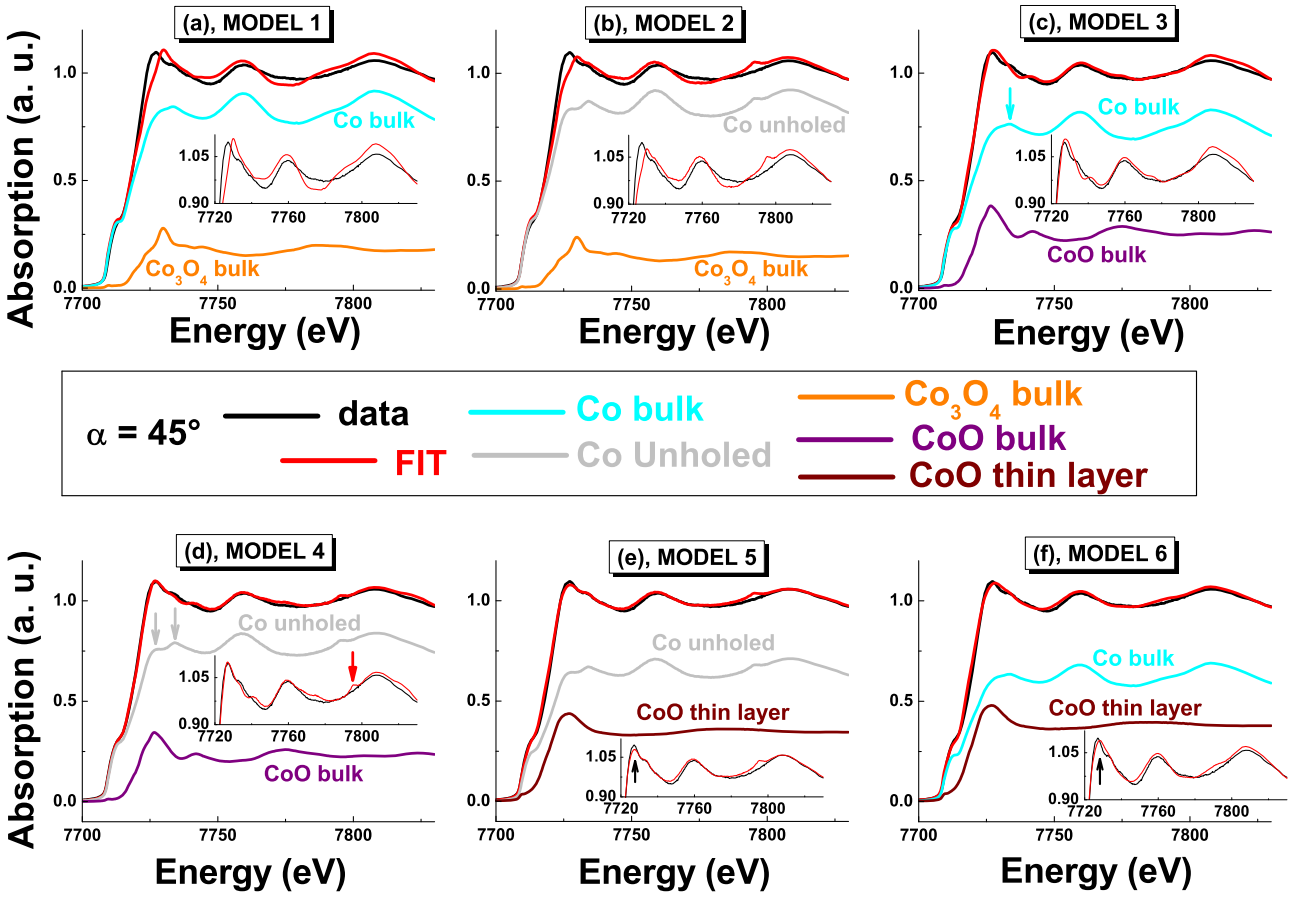

FIG. 7. LCF model fits to the normalized Co K-edge XANES spectra of the antidot with $d = 78.2$ nm (obtained at $\alpha = 45°$). The 6 different LCF models (red lines) are based on a linear combination of two reference spectra (one for metallic Co end member and one for the Co oxide end member, as indicated in the legend on the right) to fit the sample spectrum (black lines) [(a)–(f), models 1–6; see also Table I]. Insets in each figure show zooms in the normalized $\mu(E)$ region between 0.9–1.12 to highlight the quality of each fit. The reduced χ^2 parameter is a measure of the quality of the fit and is displayed above each figure.

Fig. 7(c)]. The bulk and the unholed spectrum exhibit several differences in distinct spectral features. For example, a small glitch at $E \approx 7795$ eV and a double peak around the first XANES oscillation (for $E \approx 7727.0$ eV and 7734.3 eV) are only apparent in the unholed Cu/Co/Cu spectrum, highlighted with an arrow in Fig. 7(d). The Co bulk spectrum exhibits an additional small elevation, after the first XANES peak, centered around $E \approx 7733.7$ eV, as seen in Fig. 7(c). This additional peak may originate hcp Co contributions inside the layer probe by the present 45° polarized XAS geometry. Indeed, hcp Co is sensitive to the measurement geometry and exhibits a first XANES peak doublet for polarized XAS measurements close to $\alpha = 0°$ (Ref. [51]) while a single first XANES peak is observed for high angles of 70° and 80° (Ref. [51] and present study). The same observations are obtained for our samples in the case of $\alpha = 80°$ as developed further in the paper. Clearly, this reason can be excluded. Indeed, these differences might be explained by structural differences such as Co-Cu bonds, or characteristic thin layer bonding environments in general, which lead to a modification of XANES. Since the unholed Cu/Co/Cu multilayer spectrum reproduces best the modulations of different oscillations of

TABLE I. Six different models used for adjusting the XANES profile for the 78.2 nm antidot by taking into account a linear combination of Co and oxide components. Columns: Number of model, nature of pure and oxidized Co, χ^2, pure and oxidized Co content in percent. The values in parentheses indicate the errors.

Considered model	Pure and oxidized Co	χ^2	Co content (%)	Oxide content (%)
1	Co and Co_3O_4 bulks	0.408	82.4 (1.1)	17.6 (1.1)
2	Co unholed and Co_3O_4 bulk	0.317	84.8 (1.0)	15.2 (1.0)
3	Co and CoO bulks	0.049	74.6 (0.4)	25.4 (0.4)
4	**Co unholed and CoO bulk**	**0.029**	**77.2** (0.3)	**22.8** (0.3)
5	Co unholed and CoO thin layer	0.050	65.4 (0.6)	34.6 (0.6)
6	Co bulk and CoO thin layer	0.080	62.1 (00.7)	37.9 (0.7)

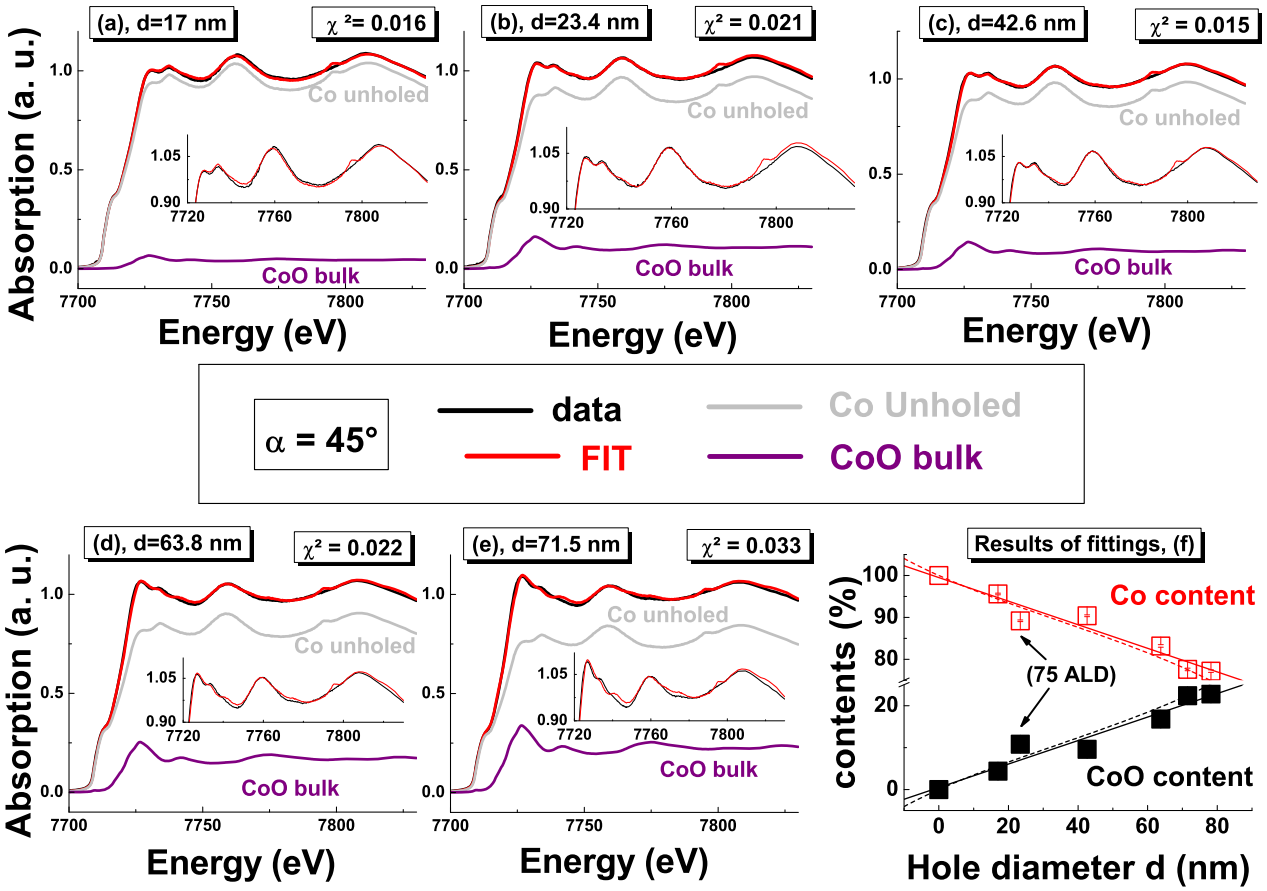

FIG. 8. (a)–(e) Data and simulated Co K-edge EXAFS profiles for Cu(10 nm)/Co(12 nm)/Cu(10 nm) sputtered on alumina membranes for different pore diameters d in the (17.0–71.5) nm range. Zooms in the (0.9–1.12) y-axis range are also shown to highlight the good quality of fits. The model is based on a sum of 2 components of absorption, unholed Cu/Co/Cu and bulk CoO components of absorption. (f) Co and CoO contents deduced from these fits are plotted as a function of d. In dotted line are represented the CoO and Co contents calculated from a model developed further [see Eq. (8)]. Here, $\alpha = 45^\circ$ and χ^2 are also given in (a)–(e).

sample spectra, it was used as the end member in the LCF analysis.

We found that the degree of oxidation obtained with different end member spectra directly relates to the quality of the fit. Oxide contents of models with poor fit quality are generally underestimated (models 1 and 2). Oxide contents obtain using the CoO thin layer reference spectrum in turn are elevated (model 5 and 6) and are close to those from edge energy fitting. For the best-fit LCF model (model 4), we obtained oxide content that is in good agreement with the one obtained from the white line fitting, i.e., 22.8(±1)% and 24.2(±1)%, respectively.

Because of the good fit quality, the unholed multilayer and bulk CoO were used as end-members to extract relative contents of metallic and oxidized Co in all other antidot samples. The LCF fitting results are presented in Fig. 8 together with the χ^2 values. As for Fig. 7, the models based on bulk Co and/or CoO thin layers are less relevant for describing the data (curves not shown). A good agreement was obtained for all antidot spectra with χ^2 being below 0.033. An increase of the χ^2 with the oxide content and pore diameter is noted. This result may indicate that our oxide reference compound cannot reproduce with a high degree of accuracy the XANES features. We therefore conclude that the oxide bonding environment in the ultrathin pores may differ from those of bulk CoO. This may suggest that oxidation in our samples takes place only on the surface of exposed ultrathin Co layers inside the pores. Moreover, as seen in these figures, the higher the pore diameter, the stronger the oxide component. The reason is the progressive oxidation of Co around the pores, causing CoO nanopores. At the same time, χ^2 weakly increases with d. This slight increase is simply understood by the existence of pores which makes slightly more difficult the model by including unholed Cu/Co/Cu and bulk CoO. Finally, the values of oxidized CoO content c(CoO) deduced from the fittings are plotted as a function of pore diameter d in Fig. 8(f). These values of c(CoO) are consistent with those appearing in the bottom right part of Fig. 5, coming from the analysis of the white line. This indicates that the 2 analyses lead to the same result. The linear variation of c(CoO) as well as c(Co), appearing in the straight line in Fig. 8(f), are found as the form [Eq. (4) and Eq. (5)]

$$c(\mathrm{CoO})(\%, \pm 0.5) = 0.28d + 0.49, \tag{4}$$

$$c(\mathrm{Co})(\%, \pm 0.5) = -0.28d + 99.50. \tag{5}$$

A comparable law is obtained from the study of the white line for CoO: $c(\mathrm{CoO})(\%, \pm 1) = 0.31 \times d$, which makes our

analysis of XANES by two different methods more robust. From the analysis of the white line as well as the edge energy, only c(CoO) is derived, whereas both c(Co) and c(CoO) are extracted from the LCF method using the absorption signal in the (7700–7830) eV range of energy. This model is valid for $d \geqslant 17$ nm since we have used the $d = 0$ membrane in our model of linear combination of absorption [Eq. (3)]. Nevertheless, we remark that for $d = 0$ in Eq. (4) and Eq. (5), expected values for Co ($\approx$1) and CoO ($\approx$0) contents are obtained. To reiterate, the main result is the progressive oxidation of antidots from air oxidation when d is raised. As a consequence, the quantity of oxidized Co is tuned by the value of the pore diameter. The same result, seen for the $d = 23.4$ nm membrane in Fig. 5, is also observed in Fig. 8. By using the atomic layer method, deposition of oxygen at the top of the layer is more favored. As a result, the oxidation of Co is more efficient especially around the pores. This might explain the increase of exchange bias at low temperature for this membrane, as detailed in another paper [44]. In fact, at room temperature, the enhancement of the coercivity is due to the pinning effects. As developed in another paper [44], exchange bias effects are revealed by lowering the measurement temperature, due to the antiferromagnetic coupling between CoO localized in the valley of nanopores and unoxidized Co on the top of membranes.

An important remark is given about the validity of the linear combination fitting concerning the choice of the references. The model is tested in that study for the best following references: CoO bulk for CoO and unholed membrane for Co. In fact, the CoO right reference is difficult to be found, due to the fact that for instance the oxidation of the pore material is disordered (vacancies might be formed in the valley of membranes). This aspect leads to the fitted XANES measurements slightly differing from the experimental ones. Nevertheless, at the end, our model persists in being valid with the employed references, and for other studies, the choice of appropriate references appears to be important.

IV. LOCAL ANTIDOT STRUCTURE AND MORPHOLOGY

The oxidation of antidots when exposed to air has been previously reported [41] from the investigation of magnetic properties and was proposed to be due to the presence of ultrathin deposition layers inside the pores, which preferentially oxidize. In the present paper, the XANES results definitely confirm the presence of oxidized Co in antidots. Indeed, the thickness variation of the deposit trilayer inside the pore exhibits most likely a crescent shape gradient, which has been also proposed in Refs. [46,47]. It is therefore likely that oxidation preferentially occurs in the vicinity of the opening of the nanopores, where the thickness of the protective Cu layer is reduced. Here, we observed the increase of the oxide content with increasing pore size from three different analysis methods of distinct XANES features. Another important result of this study is the discrepancies between the oxide component in the XANES spectra and the chosen CoO bulk reference in the LCF analysis from a quantitative analysis of absorption spectra. Nevertheless, the bulk CoO reference cannot fully reproduce the total absorption signal of the XANES spectra. This indicates that CoO possibly forms on the surface and as nanoclusters on the ultrathin metallic Co layers. Such a scenario is also consistent with the presence of CoO nanorings forming around the pores due to contact with air. The linearity between oxide content and pore diameter further indicates that the hyperfine Co layer inside the pores increases with increasing pore diameter d as the free surface area of the uncovered Co layer increases.

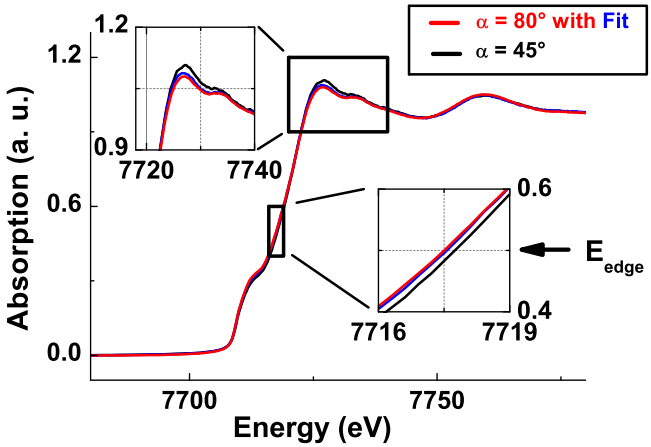

FIG. 9. Co K-edge XANES normalized profiles for an antidot sputtered on alumina membranes for $d = 78.2$ nm, for out-of-plane ($\alpha = 80°$) and intermediate ($\alpha = 45°$) polarization geometries. The angle α is the angle between the layer plane and the x-ray polarization vector $\vec{\epsilon}$. Note some differences in data around the white lines and the edge energy (two insets). The curved blue line corresponds to a fit of the $\alpha = 80°$ measurement (in red) with a linear combination of CoO bulk and unholed Cu/Co/Cu.

A. Polarized XAS observations

Polarized XAS is a powerful tool to characterize in detail anisotropic bonding environments [52], in our case the surface oxidation of Co inside the nanopores and the inclination of this oxidized layer inside the pores. As outlined in Fig. 3, we have performed polarized XAS measurements in 45° and 80° geometries. Due to the presence of pores which exhibit multilayer surfaces on their walls that are most likely inclined [46,47], we need to distinguish additionally two environments: the Co on the top of the surface (namely Co_{top}) and Co inside the pores (namely Co_{pore}). For $\alpha = 45°$, an average of perpendicular and parallel bonds to the substrate surface is sampled, while bonds perpendicular to the substrate surface are sampled for $\alpha = 90°$. Indeed, the contribution of the surface atoms on the total XAS signal is as important as the measurement is performed under grazing incidence. Figure 9 compares the XANES signals obtained in 45° and 80° geometries (black and red spectra, respectively) for the sample with the greatest pore diameter ($d = 78.2$ nm), since this sample exhibits the highest degree of oxidation and therefore might show the greatest differences in XANES between the two geometries.

It seems that there is no preferential orientation of our Co antidots due to weak differences between the two absorption signals recorded for the 2 angles [53]. Nevertheless, we observe several distinct modifications of the absorption signal between the two geometries, including a shift of the edge energy to

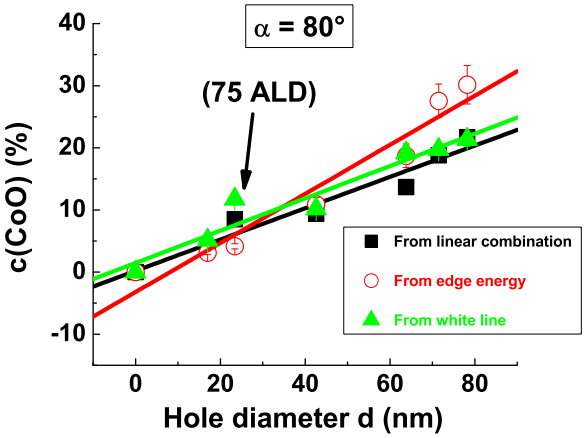

FIG. 10. CoO content deduced from 3 different procedures (edge energy, while line, and linear combination) as a function of pore diameter d for antidots sputtered on alumina membranes, for an out-of-plane ($\alpha = 80^\circ$) polarization geometry. $d = 0$ corresponds to the unholed multilayer.

lower energies, a decrease of the white line intensity, as well as a decrease of the amplitude of the first EXAFS oscillation when changing from the 45° to the 80° geometry (see the 2 insets in Fig. 9). These differences may indicate a higher degree of oxidation probed in the 45° measurement geometry compared to 80°. This finding indicates that the oxidation of Co is preferentially located in the vicinity of nanopores.

We determined the oxide content in the spectra obtained in the 80° geometry using the same three methods and approaches as outlined above for the spectra collected 45°, including the variations of WL intensities, edge energy position, as well as the LCF analysis. Derived relations between c(CoO) and pore diameter d for the 80° geometry samples are presented in Fig. 10. Similarly to the results obtained in 45°, all methods reveal a linear relation between c(CoO) and d. Moreover, also in the 80° geometry the edge energy method leads to overestimated sample oxidation states compared to the WL analysis and LCF procedure. Finally, derived slopes of c(CoO) versus d from the three methods are smaller for spectra measured in 80° geometry compared to those measured in the 45° geometry. For example, the oxide content of the sample with $d = 78.2$ nm shown in Fig. 10 is slightly lower in 80° compared to the 45° geometry, decreasing from 22.8(0.6) to 21.7(0.6).

The differences between the XANES and degree of oxidation obtained in the two geometries can be related to different bond directions probed inside the pores (Co_{pore}). Indeed, the oxidation of Co on top of the substrate can be neglected because the Cu deposited layer remains thick at this location and therefore prevents any oxidation. Moreover, the linear increase of the oxide content with pore diameter suggests the oxidation of pore surfaces and the formation of nanorings. At the K edge the photoelectron probes the Co p orbitals parallel to the polarization direction of the beam. In the 80° geometry mainly intralayer bonds are probed that are dominated by Co-Co bonds as derived oxide contents are smaller. In contrast, in 45° in which a higher degree of oxidation has been obtain, Co p orbitals perpendicular to the thin layer surface are probed, which therefore have to be composed of mainly Co-O bonds. The later observation confirms that oxidation takes place only on the inner pore surfaces at the exposed ultrathin Co layer (Co_{pore} oxidized in part with oxygen). Moreover, even if the sample is probably polycrystalline (no preferential direction due to the sputtering process), the observations also indicate an inclination of this layer relative to the substrate surface which is in agreement with the crescent shape proposed in earlier works.

The determined relations between CoO contents and pore diameter d extracted from the three different analysis methods and for spectra collected in the two different geometries are summarized in Table II. We have obtained very good least-squares fits to the XANES spectra by using a linear combination of reference spectra, similarly to Ref. [43]. We believe that the linear combination analysis provides a very good estimation of metallic and oxidized Co contents. Our confidence in this model comes the large range of energy and the appropriate reference compounds used in the linear combination method. Moreover, structural investigations performed by polarized XANES studies confirm that Co oxidation preferentially forms at the surface of the inner pore walls.

B. Antidot morphology

Atomic force microscopy (AFM) is another tool used to gain a more detailed local picture of nanometric surface features of antidots. An AFM topography map for a moderate pore diameter is presented in Fig. 11(a). The pore diameter is close to the measured one by SEM ($d \approx 60$ nm). Consistent also with SEM observations, a regular hexagonal arrangement of nanopores ($p \approx 105$ nm) on the membrane surfaces is evident in the AFM map. In fact, as pointed out by [38], due to the limited detecting ability of the atomic force microscope technique into the nanopores, only the top part of the membrane, as well as the partial view of nanopores, can be imaged by this method. Indeed, the deposition in the antidot arrays is mainly on the

TABLE II. Co and CoO contents, evaluated from 3 different methods using the position of the edge energy, the white line, and a linear combination of adapted references, versus the pore diameter d. Here, intermediate ($\alpha = 45^\circ$) and out-of-plane ($\alpha = 80^\circ$) polarization geometries are chosen. The values in parentheses indicate the errors.

α (polarization geometries)	from the edge energy (±2%)	from the white line (±1%)	from a linear combination (±0.5%)
45°	$c(\mathrm{CoO}) = 0.44 \times d$	$c(\mathrm{CoO}) = 0.31 \times d$	$c(\mathrm{CoO}) = 0.28 \times d + 0.49c(\mathrm{Co}) = -0.28 \times d + 99.50$
80°	$c(\mathrm{CoO}) = 0.40 \times d - 3.22$	$c(\mathrm{CoO}) = 0.26 \times d + 1.47$	$c(\mathrm{CoO}) = 0.25 \times d + 0.19c(\mathrm{Co}) = -0.25 \times d + 99.81$

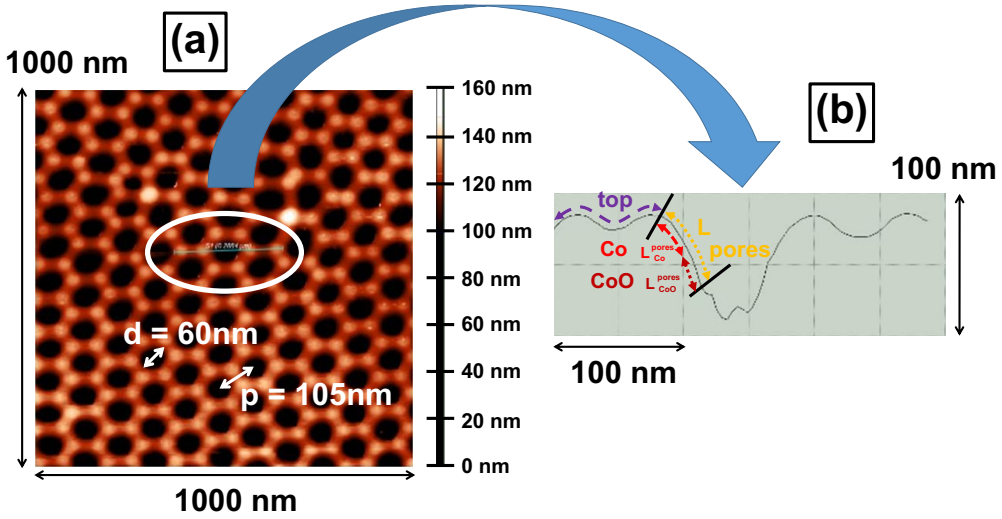

FIG. 11. (a) Top-view AFM map of sample $d = 63.8$ nm (corresponding to $t_{\text{etching}} = 60$ minutes) of a surface area of 1000×1000 nm^2 having a depth resolution of 160 nm. The vertical dimension is expressed as color scale with white being the uppermost and black being the lowest portions of the sample. Note the hexagonal arrangement of holes and the secondary hexagonal pattern of the nanohills (white dots). (b) Schematic cross section in the (x,z) plane through a nanohole and adjacent nanohill structures. Abbreviations are as follows: top, Co layer on substrate surface; L, total length of Co layer in the inner hole walls; $L_{\text{Co}}^{\text{pores}}$, length of the unoxidized Co layer along the hole walls; $L_{\text{CoO}}^{\text{pores}}$, length of the oxidized Co layer in deeper portions of the nanoholes. Here, $L = L_{\text{Co}}^{\text{pores}} + L_{\text{CoO}}^{\text{pores}}$. Note the nanohill doublet seen on the side of the hole that has a periodicity of 500 nm.

top and the inner wall of the templates, since the diameter is in the nanometric range and the height in the micrometer regime. Consequently, no deposited material can reach the bottom of the pores. Interestingly, a secondary hexagonal network around each nanopore can be distinguished on the substrate surfaces, which is composed of 6 white point first neighbors surrounding the pore [white dots in Fig. 11(a); see also color scale on the right]. Figure 11(b) shows a schematic cross section through a nanopore in the (x,z) plane together with the surrounding substrate surface [see the straight line in Fig. 11(a)]. The antidot surface appears to be modulated with a periodic length of the nanohills of ≈50 nm, which is similar to AFM observations reported in [54]. The height of nanohills relative to the substrate surface reaches between 15 nm as deduced from this scale, which is in agreement with previous observations [38,54].

It is well known that the topography of anodic alumina membranes is composed of both nanopores as well as surrounding nanohills (see for example Refs. [5,38,39,54–56]). This particular deposition is often observed together with the appearance of the crescent shape of the multilayer deposit inside the nanopores, as previously assumed in our antidots [41] and detailed in [12]. The reason might be explained by the double-anodization technique which induces alumina nanohills on the top of membranes. Artifacts caused by the tip shape could induce particular topology of the antidots, as revealed by the AFM view of Fig. 11(b). Consequently, conclusions about the morphology around the pores have to prudently be discussed. Nevertheless, additional investigations performed by SEM when the sample is tilted confirm the crescent shape of the antidots (views not shown). In addition, the curvature of the nanoholes is well described by transmission electron microscope measurements for similar antidots studied in the literature [31,35].

V. A MORPHOLOGICAL MODEL

A. Model

Unfortunately, it appears to be difficult to evaluate both the nature and the quantity of materials along the walls of antidots. As a consequence, an open question is the comparison of the two deposited quantities: one on the top of the antidot (on the undulated antidots) and the second one on the walls of membranes [inclined as sketched in Fig. 11(b)]. The detailed knowledge on the extent and chemical nature of the CoO layer inside the pores is crucial for understanding the nanomagnetic properties of antidots [44]. Specifically, the direction of magnetic moments is directly related to antidot morphology and chemical composition. Thus, to refine our current picture on the oxidation of ultrathin sputtered transition-metal layers (i.e., Co or Fe) inside nanopores in general, we developed a method to calculate the quantity of material deposited on the substrate surfaces and inner antidot pore wall. Finally we used the model to determine the fraction of deposited material on top of the antidot surface, which is of general interest for antidots.

In our model, we assumed a flat sample surface area S_o of 1 cm^2, for the top part of antidots, for simplicity of calculations. The density of pores [namely density(pores)] can then be expressed as density(pores) $= 1/(p^2)$ due to the symmetric hexagonal arrangement of pores as observed from AFM and SEM investigations. The surface area of metallic Co sputtered only on the substrate surface [see this surface on the top of antidots in Fig. 11(b)] can be calculated from $S_{\text{Co}}^{\text{top}} = S_o -$ density(pores) $\times\, \pi(d^2)/4$, with $\pi(d^2)/4$ the surface area of one pore. Substituting S_o and density(pores) for our model we derive $S_{\text{Co}}^{\text{top}} = 1 - \pi(d/2p)^2$ as the surface area of the membrane without pores (with p the period, 105 nm in our case). The total penetration length (L) of the deposited Co layer along the inner pore wall is obtained from $L = L_{\text{Co}}^{\text{pores}} + L_{\text{CoO}}^{\text{pores}}$

with $L_{\mathrm{Co}}^{\mathrm{pores}}$ being the length of the unoxidized Co layer that is covered with a sufficiently thick Cu layer, and $L_{\mathrm{CoO}}^{\mathrm{pores}}$ being the length of the oxidized Co layer exposed to air. L, $L_{\mathrm{CoO}}^{\mathrm{pores}}$, and $L_{\mathrm{CoO}}^{\mathrm{pores}}$ are sketched in Fig. 11(b). The total surface of Co sputtered on the inner pore walls can be calculated from $S_{\mathrm{Co}}^{\mathrm{pores}} = (\pi d \times L_{\mathrm{Co}}^{\mathrm{pores}})/(p^2)$. The total surface of the Co layer $S_{\mathrm{Co}}^{\mathrm{Total}}$ can then be expressed as

$$S_{\mathrm{Co}}^{\mathrm{Total}} = 1 - (\pi/4) \times (d/p)^2 + \left(\pi d \times L_{\mathrm{Co}}^{\mathrm{pores}}\right)/(p^2). \quad (6)$$

As CoO is expected to form only at the deeper portions of the pore walls along $L_{\mathrm{CoO}}^{\mathrm{pores}}$, we derive in the same way as for $S_{\mathrm{Co}}^{\mathrm{Total}}$

$$S_{\mathrm{CoO}}^{\mathrm{Total}} = \left(\pi d \times L_{\mathrm{CoO}}^{\mathrm{pores}}\right)/(p^2). \quad (7)$$

In the following we further assume that the thickness of the Co layer remains constant over the length L. Based on this assumption the Co and CoO contents can be derived from $c(\mathrm{Co}) = S_{\mathrm{Co}}^{\mathrm{Total}}/(S_{\mathrm{Co}}^{\mathrm{Total}} + S_{\mathrm{CoO}}^{\mathrm{Total}})$ and $c(\mathrm{CoO}) = S_{\mathrm{CoO}}^{\mathrm{Total}}/(S_{\mathrm{Co}}^{\mathrm{Total}} + S_{\mathrm{CoO}}^{\mathrm{Total}})$, respectively. Substituting $S_{\mathrm{Co}}^{\mathrm{Total}}$ and $S_{\mathrm{CoO}}^{\mathrm{Total}}$ we can bring the concentrations in relationship with the pore diameter d as well as the pore periodicity p [Eq. (8) and Eq. (9)]:

$$c(\mathrm{CoO}) = \frac{1}{1 + \left[p^2/(\pi d) - d/4 + L_{\mathrm{Co}}^{\mathrm{pores}}\right]/\left(L_{\mathrm{CoO}}^{\mathrm{pores}}\right)}, \quad (8)$$

$$c(\mathrm{Co}) = \frac{1}{1 + \left(L_{\mathrm{CoO}}^{\mathrm{pores}}\right)/\left[p^2/(\pi d) - d/4 + L_{\mathrm{Co}}^{\mathrm{pores}}\right]}. \quad (9)$$

In the above expressions we obtain $c(\mathrm{CoO}) = 0$ and $c(\mathrm{Co}) = 1$ when d equals 0. Moreover, both $c(\mathrm{CoO})$ and $c(\mathrm{Co})$ increase and decrease progressively with d, which is consistent with the present structural model and the assumed location of CoO in the deeper parts of the pore walls [Fig. 11(b)]. The unknown parameters in Eq. (8) and Eq. (9) are the lengths of the metallic Co layer on the pore rims $L_{\mathrm{Co}}^{\mathrm{pores}}$ as well as the length of the oxidized Co layer inside the pore $L_{\mathrm{CoO}}^{\mathrm{pores}}$. We estimated $L_{\mathrm{Co}}^{\mathrm{pores}}$ and $L_{\mathrm{CoO}}^{\mathrm{pores}}$ by fitting the experimental data plotted in Fig. 8(f) with these two equations (p is fixed at 105 nm in the equations). We want to point out that the fits are performed on both $c(\mathrm{CoO})$ and $c(\mathrm{Co})$ curves, leading to the same lengths. The high-quality adjustments appear in dotted lines in this figure. We find values of $L_{\mathrm{CoO}}^{\mathrm{pores}}$ and $L_{\mathrm{Co}}^{\mathrm{pores}}$ of 11.8 nm and 14.1 nm, resulting in a total length of $L \approx 26$ nm. This result is in very good agreement with the maximal penetration depth (L) of 30 nm suggested for sputtered multilayers by Sousa *et al.* [5] and also reported by Ref. [57]. This agreement suggests that the present structural model is appropriate to calculate the length of the metallic and oxidized Co layer inside the nanopores.

Two assumptions have been made in this model: (i) the observed nanohill morphology on the substrate surface is not taken into account and only a flat surfaces is considered; and (ii) in a first approximation the layer thickness was assumed to be uniform. We however found that the inclusion of nanohill structures into the total surface area may only slightly modify the results. If the crescent shape of the multilayer inside the pores is taken into account in turn, the model will give higher values for the total length and therefore for both $L_{\mathrm{CoO}}^{\mathrm{pores}}$ and $L_{\mathrm{Co}}^{\mathrm{pores}}$ of approximately 50%, due to the conservation of volume. For instance, an increase of $L_{\mathrm{CoO}}^{\mathrm{pores}}$ and $L_{\mathrm{Co}}^{\mathrm{pores}}$ by 50%, i.e., ≈17.7 nm and ≈21 nm, respectively will lead to a total length L of ≈40 nm.

It is also interesting to evaluate the relative proportions of Co atoms deposited inside the nanopores versus those on the top of membranes, namely c_{walls} and c_{top}, respectively. In the present study, the walls of the nanopores are composed of both metallic Co and CoO and participate in the c_{walls} value, whereas only metallic Co is deposited on the top of antidots and contributes to c_{top}. Starting from the calculations developed above, c_{walls} and c_{top} can be easily expressed by the following equations:

$$c_{\mathrm{top}} = \frac{S_{\mathrm{Co}}^{\mathrm{top}}}{S_{\mathrm{Total}}} = \frac{1 - (\pi/4)(d/p)^2}{S_{\mathrm{Total}}}, \quad (10)$$

$$c_{\mathrm{walls}} = \frac{S_{\mathrm{Co,CoO}}^{\mathrm{walls}}}{S_{\mathrm{Total}}} = \frac{\pi d L/p^2}{S_{\mathrm{Total}}}, \quad (11)$$

where $S_{Total} = 1 - \pi(d/2p)^2 + \pi d L/(p)^2$. These equations can be applied to calculate proportions of deposited material inside the pores and on top for any antidot with pore diameter since then d and period p are known. For instance, in the case of our antidots, c_{walls} varies from 16% to 61% when d is enhanced from 17 nm to 68 nm. This result indicates the important influence of atoms deposited on the walls of antidots for the highest d value.

Our model could be easily used in the literature for estimating atomic fractions around nanoholes and on the top of membranes. An important remark has to be discussed about the fact that atoms might be deposited by deposition methods using a more favored direction (for instance perpendicular to the layers), such as the e-beam technique. In that case, the deposition of material inside the pores is suspected to be minimal. Nevertheless, our model persists in being applied, resulting in atomic proportions more weak in the valley of nanopores compared to ones found in that present study (using the sputtering technique less directional).

B. Comparison model/experiments

In the following we compare the p/d ratios to the maximum and minimum values of c_{walls} and c_{top} obtained from our models to experimental findings of this study and those reported in the literature (Table III). For the calculation, a penetration depth of $L = 40$ nm was assumed. We observe, as expected, that the maximum (minimum) of c_{walls} and minimum (maximum) of c_{top} are directly related to the lowest (highest) p/d ratio.

In order to understand the effect of these quantities on the antidot properties we listed additionally the maximum and minimum ambient temperature coercivities (H_C^{max} and H_C^{min}) of holed antidots and unholed templates (in parentheses) in Table III. Literature values compared here are from antidot substrates that have similar multilayer thickness compared to the samples investigated in this study (indicated in bold in Table III). H_C^{min} and H_C^{max} for this study are taken for the sample with the lowest and highest pore diameter, respectively. The direction of the applied magnetic field is systematically orientated following the easy axis, except for Ref. [19]. In this last reference, the large value is explained by the loss of the perpendicular magnetic anisotropy for the high-d regime. Variations of antidot coercivities observed in Table III may however also be related to differences in stacks and in particular in the ferromagnetic or in some cases antiferromagnetic layer

TABLE III. Comparison of structural characteristic and magnetic properties of antidots reported in the literature and determined in the present study. Listed information of antidots includes type of acid used during synthesis, the multilayer system (thickness in nm), period p and pore diameter d (in nm), d/p ratio, as well as calculated proportions of material deposited on the substrate surface (c_{top}, ± 2) and walls (c_{walls}, ± 2) in percent from our model [see Eq. (10) and Eq. (11)]. Reported magnetic properties correspond to the minimum and maximum coercivity $H_C^{\min}$ and H_C^{max}, as well as the coercivity for the unholed stack in parentheses, and associated references.

Type of acid	Systems	p (nm)	d (nm)	p/d	c_{walls} (%)	c_{top} (%)	$H_C^{\min}/H_C^{max}$ at RT	References
sulfuric	$[\text{Co}(0.5)/\text{Pt}(2)]_{20}$	60	9–48	6.67/1.25	24.2/77.1	75.8/22.9	540/1350(140)	[19]
sulfuric	IrMn(8)/CoFe(**10**)	60	10–48	6.00/1.25	26.3/77.1	73.7/22.9	217/501(27)	[25]
oxalic	Co(**20**–210)	100	35–90	2.86/1.11	32.7/75.7	67.3/24.3	≈50/503(7)	[27]
oxalic	CoCrPt(**10**–20)	105	40–80	2.63/1.31	33.9/62.7	66.1/37.3	420/430(150)	[37]
oxalic	NiFe(**18**–138)	105	35–66	3.00/1.59	30.4/52.2	69.6/47.8	70/240(few Oe)	[20]
oxalic	$[\text{NiFe}(\mathbf{20}\text{–}100)/\text{FeMn}(15)]_{10}$	120	30–80	4.00/1.50	21.6/51.7	78.4/48.3	23/30(11)	[26]
oxalic	NiFe(**10**–20)	105	22–65	4.77/1.62	20.6/51.3	79.4/48.7	(few Oe)/40(not given)	[28]
oxalic	Co(12)	105	17–78	6.18/1.35	16.5/60.9	83.5/39.1	27/880(5)	present study

[25,26]. The latter may induce exchange bias effects and a potential increase in coercivity.

Nevertheless, a general observation is the significant increase of H_C with the presence of pores in the substrate. Second, H_C^{max} also increases with the proportion of material deposited inside the pores (c_{walls}). Starting from these two observations, the clear increase of the coercivity is caused by the opening of nanostructures, where the pinning of the domain walls induces a strong coupling. This leads to an increase of the coercivity H_C. In fact, the variation of H_C with the geometrical parameters, namely p and d, is assumed to be of the form $H_C = 1/(p-d)$, initially predicted by Hilzinger and Kronmüller [58]. This type of behavior is currently observed for published studies [34,36] in the literature. This is simply understood by the fact that the pinning effects become more efficient when the magnetic atoms are mainly deposited around the nanoholes. Consequently, the more d increases, the smaller the value of $p-d$ becomes, causing an enhancement of the coercivity according to the previous law. A strong magnetic field is necessary to overcome the pinning coupling.

We note also that, for the largest d value, the magnetic atomic species located around pores are dominant (50%) in the structure, leading to strong coercivity. Moreover, the ratio p/d seems also to be a key factor to relate the magnetic properties to the antidot structure. In our model the p/d ratio is directly related to c_{walls} in our model [see Eq. (11)]. Indeed, c_{walls} progressively increase with this ratio. We therefore propose that the quantities of atoms deposited on the walls of membranes strongly contribute to the enhancement of the coercivity. More details will be discussed in another paper devoted to magnetic properties of the Cu/Co/Co antidots, specially by varying both the temperature and the magnetic field (amplitude/orientation), and for a series of different pore diameters, in the light of our structural investigations. As known in the literature, and for the first time, the exchange bias effect was discovered 60 years ago by Meiklejohn and Bean [59], for CoO associated with Co, whereas the antiferromagnetic coupling is not expected when CoO is replaced by Co_3O_4. For a more comprehensive understanding of exchange bias effects, Ref. [60] reviews the phenomenology of such effects, for antiferromagnetic/ferromagnetic structures, with in particular intensive investigations using CoO as an antiferromagnetic material.

VI. CONCLUSION

We have synthesized Cu(10 nm)/Co(12 nm)/Cu(10 nm) sputtered on antidots with a range of different pore diameters d (20–80 nm). Conventional pore diameters [d = (40–80) nm] were obtained with the double-anodization technique while weaker d values (20–40 nm) could be achieved with an additional atomic layer deposition treatment of antidots. Resulting antidots exhibit a period of the array p of 105 nm. The local structural characteristics of these membranes have been investigated using polarized x-ray absorption near edge spectroscopy (XANES) as well as SEM and AFM microscopy techniques. All membranes exhibit a regular hexagonal network of pores, and only substrates treated with the ALD process show slight deviations from a circular pore shape. Polarized XANES allowed us to determine the proportions of metallic Co and CoO in different parts of the membranes. We tested three different analytical methods for this evaluation, including variation of the white line intensity as well as the edge energy, and finally the linear combination fitting procedure. We found that the latter gave the most robust results. We further found that metallic Co is the dominating species on the membrane surface as well as inside the pores. We show the formation of CoO (maximum of 25% of CoO) inside the pore walls, which appears most likely as nanorings. The CoO content increases linearly with the pore diameter. This is related to the crescent shape of the multilayer inside the pores and the reduction of thickness of the uppermost Cu layer that leads to the oxidation of the centered ultrathin Co layer when exposed to the air. We have developed a simple geometrical model to evaluate the proportions and layer length of Co and CoO on the pore rims and inside the pore walls. Moreover, we also provide a simple formula that allows us to determine the proportion of material deposited on top of the surface as well as inside the walls for any antidot from the period p, the pore diameter d, and the penetration length L [see Eq. (10) and Eq. (11)]. The physical properties of nanopores studied in the literature might be in part explained by the atomic proportions thanks to our model. In the case of our antidots, the crescent shape

of the multilayer inside the pores and the presence of CoO nanorings induce particular magnetic reversal and exchange bias effects at low temperature, as developed in a forthcoming paper.

ACKNOWLEDGMENTS

This work was supported by the French Ministry of Foreign Affairs. The authors are thankful to O. Fruchart for the AFM measurements.

[1] M. Baert, V. V. Metlushko, R. Jonckheere, V. V. Moshchalkov, and Y. Bruynseraede, Phys. Rev. Lett. **74**, 3269 (1995).
[2] M. Tornow, D. Weiss, K. v. Klitzing, K. Eberl, D. J. Bergman, and Y. M. Strelniker, Phys. Rev. Lett. **77**, 147 (1996).
[3] T. Shen, Y. Q. Wu, M. A. Capano, L. P. Rokhinson, L. W. Engel, and P. D. Ye, Appl. Phys. Lett. **93**, 122102 (2008).
[4] A. Yu. Kuntsevich, A. V. Shupletsov, and M. S. Nunuparov, Phys. Rev. B **93**, 205407 (2016).
[5] C. T. Sousa, D. C. Leitao, M. P. Proenca, J. Ventura, A. M. Pereira, and J. P. Araujo, Appl. Phys. Rev. **1**, 031102 (2014).
[6] C. C. Wang, A. O. Adeyeye, N. Singh, Y. S. Huang, and Y. H. Wu, Phys. Rev. B **72**, 174426 (2005).
[7] R. P. Cowburn, A. O. Adeyeye, and J. A. C. Bland, Appl. Phys. Lett. **70**, 2309 (1997).
[8] A. O. Adeyeye, J. A. C. Bland, and C. Daboo, Appl. Phys. Lett. **70**, 3164 (1997).
[9] L. J. Heyderman, F. Nolting, and C. Quitmann, Appl. Phys. Lett. **83**, 1797 (2003).
[10] C. C. Wang, A. O. Adeyeye, and Y. H. Wu, J. Appl. Phys. **94**, 6644 (2003); **97**, 10J902 (2005).
[11] L. Torres, L. Lopez-Diaz, and J. Iñiguez, Appl. Phys. Lett. **73**, 3766 (1998).
[12] M. T. Rahman, N. N. Shams, and C.-H. Lai, Nanotechnology **19**, 325302 (2008).
[13] D. A. Allwood, G. Xiong, C. C. Faulkner, D. Atkinson, D. Petit, and R. P. Cowburn, Science **309**, 1688 (2005).
[14] S. S. P. Parkin, M. Hayashi, and L. Thomas, Science **320**, 190 (2008).
[15] X. K. Hu, S. Sievers, A. Müller, V. Janke, and H. W. Schumacher, Phys. Rev. B **84**, 024404 (2011).
[16] A. Yu. Toporov, R. M. Langford, and A. K. Petford-Long, Appl. Phys. Lett. **77**, 3063 (2000).
[17] C. C. Wang, A. O. Adeyeye, and N. Singh, Appl. Phys. Lett. **88**, 222506 (2006).
[18] H. Masuda and K. Fukuda, Science **268**, 1466 (1995).
[19] M. T. Rahman, N. N. Shams, C. H. Lai, J. Fidler, and D. Suess, Phys. Rev. B **81**, 014418 (2010).
[20] K. J. Merazzo, D. C. Leitao, E. Jiménez, J. P. Araujo, J. Camarero, R. P. del Real, A. Asenjo, and M. Vázquez, J. Phys. D: Appl. Phys. **44**, 505001 (2011).
[21] S. Da Col, M. Marques, O. Fruchart, and L. Cagnon, Appl. Phys. Lett. **98**, 112501 (2011).
[22] V. P. Chuang, W. Jung, C. A. Ross, J. Y. Cheng, O.-H. Park, and Ho-Cheol Kim, J. Appl. Phys. **103**, 074307 (2008).
[23] Z. L. Xiao, C. Y. Han, U. Welp, H. H. Wang, V. K. Vlasko-Vlasov, W. K. Kwok, D. J. Miller, J. M. Hiller, R. E. Cook, G. A. Willing, and G. W. Crabtree, Appl. Phys. Lett. **81**, 2869 (2002).
[24] F. J. Castaño, K. Nielsch, C. A. Ross, J. W. A. Robinson, and R. Krishnan, Appl. Phys. Lett. **85**, 2872 (2004).
[25] N. N. Shams, M. T. Rahman, and C. H. Lai, J. Appl. Phys. **105**, 07D722 (2009).
[26] N. N. Phuoc, S. L. Lim, F. Xu, Y. G. Ma, and C. K. Ong, J. Appl. Phys. **104**, 093708 (2008).
[27] Y. H. Jang and J. H. Cho, J. Appl. Phys. **115**, 063903 (2014).
[28] K. J. Merazzo, C. Castán-Guerrero, J. Herrero-Albillos, F. Kronast, F. Bartolomé, J. Bartolomé, J. Sesé, R. P. del Real, L. M. García, and M. Vázquez, Phys. Rev. B **85**, 184427 (2012).
[29] C. Jiang, Q. Liu, R. Liu, J. Wang, and D. Xue, Thin Solid Films **515**, 6967 (2007).
[30] A. Maximenko, J. Fedotova, M. Marszalek, A. Zarzycki, and Y. Zabila, J. Magn. Magn. Mater. **400**, 200 (2016).
[31] M. T. Rahman, R. K. Dumas, N. Eibagi, N. N. Shams, Y.-C. Wu, K. Liu, and C.-H. Lai, Appl. Phys. Lett. **94**, 042507 (2009).
[32] M. T. Rahman, N. N. Shams, and C.-H. Lai, J. Appl. Phys. **105**, 07C112 (2009).
[33] B. J. Kirby, M. T. Rahman, R. K. Dumas, J. E. Davies, C. H. Lai, and K. Liu, J. Appl. Phys. **113**, 033909 (2013).
[34] P. Prieto, K. R. Pirota, M. Vazquez, and J. M. Sanz, Phys. Status Solidi A **205**, 363 (2008).
[35] W. J. Gong, W. J. Yu, W. Liu, S. Guo, S. Ma, J. N. Feng, B. Li, and Z. D. Zhang, Appl. Phys. Lett. **101**, 012407 (2012).
[36] K. Pirota, P. Prieto, A. Neto, J. Sanz, M. Knobel, and M. Vazquez, J. Magn. Magn. Mater. **320**, e235 (2008).
[37] D. Navas, F. Ilievski, and C. A. Ross, J. Appl. Phys. **105**, 113921 (2009).
[38] W. J. Gong, W. Liu, J. N. Feng, D. S. Kim, C. J. Choi, and Z. D. Zhang, J. Appl. Phys. **115**, 133909 (2014).
[39] M. Jaafar, D. Navas, A. Asenjo, M. Vázquez, M. Hernández-Vélez, and J. M. García-Martín, J. Appl. Phys. **101**, 09F513 (2007).
[40] N. A. Kulesh, M. Vázquez, V. N. Lepalovskij, and V. O. Vas'kovskiy, Nanotechnology **29**, 065301 (2018).
[41] F. Fettar, L. Cagnon, and N. Rougemaille, Appl. Phys. Lett. **97**, 192502 (2010).
[42] O. Bezencenet, H. Magnan, C. Mocuta, E. Fonda, S. Stanescu, P. Ohresser, R. Belkhou, and A. Barbier, Phys. Rev. B **81**, 085419 (2010).
[43] S. Couet, K. Schlage, K. Saksl, and R. Rohlsberger, Phys. Rev. Lett. **101**, 056101 (2008).
[44] H. Garad, S. Usmani, D. Barral, P. David, L. Cagnon, D. Testemale, D. Mannix, O. Proux, A. Rosa, O. Mathon, S. Pascarelli, and F. Fettar (unpublished).
[45] B. Ravel and M. Newville, J. Synchrotron Radiat. **12**, 537 (2005).
[46] L. Balcells, B. Martinez, O. Iglesias, J. M. García-Martín, A. Cebollada, A. García-Martín, G. Armelles, B. Sepúlveda, and Y. Alaverdyan, Appl. Phys. Lett. **94**, 062502 (2009).
[47] W. O. Rosa, L. Martínez, M. Jaafar, A. Asenjo, and M. Vázquez, J. Appl. Phys. **106**, 103906 (2009).
[48] H. Garad, L. Ortega, A. Y. Ramos, Y. Joly, F. Fettar, S. Auffret, B. Rodmacq, B. Dieny, O. Proux, and A. I. Erko, J. Appl. Phys. **114**, 053508 (2013).
[49] Y. Joly, Phys. Rev. B **63**, 125120 (2001).

[50] J. J. Rehr, J. J. Kas, F. D. Vila, M. P. Prange, and K. Jorissen, Phys. Chem. Chem. Phys. **12**, 5503 (2010).
[51] P. Le Fevre, H. Magnan, O. Heckmann, V. Briois, and D. Chandesris, Phys. Rev. B **52**, 11462 (1995).
[52] C. Lamberti, Surf. Sci. Rep. **53**, 1 (2004).
[53] P. LeFevre, H. Magnan, and D. Chandesris, Surf. Sci. **352-354**, 923 (1996).
[54] D. C. Leitao, J. Ventura, C. T. Sousa, J. M. Teixeira, J. B. Sousa, M. Jaafar, A. Asenjo, M. Vazquez, J. M. De Teresa, and J. P. Araujo, Nanotechnology **23**, 425701 (2012).
[55] D. C. Leitao, A. Apolinario, C. T. Sousa, J. Ventura, J. B. Sousa, M. Vazquez, and J. P. Araujo, J. Phys. Chem. C **115**, 8567 (2011).
[56] F. Beron, K. R. Pirota, V. Vega, V. M. Prida, A. Fernandez, B. Hernando, and M. Knobel, New J. Phys. **13**, 013035 (2011).
[57] Y. Lei and W.-K. Chim, Chem. Mater. **17**, 580 (2005).
[58] H. R. Hilzinger and H. Kronmüller, J. Magn. Magn. Mater. **2**, 11 (1976).
[59] W. H. Meiklejohn and C. P. Bean, Phys. Rev. **102**, 1413 (1956). **7**
[60] J. Nogués and I. K. Schuller, J. Magn. Magn. Mater. **192**, 232 (1999). **Q**